Article

Not peer-reviewed version

Optimization for Removal Characteristics of Cage Net Fouling by Low-Pressure Abrasive Water Jet Based on Response Surface Methodology and Entropy Method

Yingjie Wu , Yongqiang Tu , Bin Deng , Hui Li , Guohong Xiao * , Hu Chen *

Posted Date: 22 October 2025

doi: 10.20944/preprints202510.1743.v1

Keywords: LPAWJ; numerical simulation; Box-Behnken response surface methodology; entropy method

Article

Optimization for Removal Characteristics of Cage Net Fouling by Low-Pressure Abrasive Water Jet Based on Response Surface Methodology and Entropy Method

Yingjie Wu [1], Yongqiang Tu [1,2,3], Bin Deng [1], Hui Li [1,2,3], Guohong Xiao [1,2,3,*] and Hu Chen [1,2,3,*]

[1] College of Marine Equipment and Mechanical Engineering, Jimei University, Xiamen 361021, China

[2] Key Laboratory of Ocean Renewable Energy Equipment of Fujian Province, Xiamen, 361021, China

[3] Key Laboratory of Energy Cleaning Utilization and Development of Fujian Province, Xiamen, 361021, China

* Correspondence: 541153203@qq.com (G.X.); 200661000006@jmu.edu.cn (H.C.); Tel.: +86-13328304072(G.X.); +86-13696946391(H.C.)

Abstract

Deep-sea cages are highly susceptible to biofouling due to long-term seawater immersion, which promotes the attachment and growth of marine organisms on nets, significantly reducing fish survival. To address this issue, this study explores the use of low-pressure abrasive-water jets (LPAWJ) for cage fouling removal through numerical simulation. Based on a Box-Behnken response surface design, nozzle inlet pressure X_1, nozzle outlet diameter X_2, and target distance X_3 were selected as optimization parameters. The peak jet impact force Z_1, stable jet impact force Z_2, peak abrasive-water jet velocity Z_3, and peak abrasive particle velocity Z_4 were chosen as evaluation indicators to characterize the jet's instantaneous impact ability, sustained action ability, and dynamic particle behavior. Using the entropy method, weights for each indicator were determined, and the jet's overall removal capability was calculated. A regression model was developed by integrating numerical simulation with the response surface methodology (RSM), and the optimal parameter combination was identified as X_1 = 4.5 MPa, X_2 = 10 mm, and X_3 = 205.396 mm, enhancing the jet's overall removal capability by 2.19%. The results provide theoretical support for improving LPAWJ-based cage net cleaning.

Keywords: LPAWJ; numerical simulation; Box-Behnken response surface methodology; entropy method

1. Introduction

Since the Reform and Opening-up, China's mariculture industry has developed rapidly, driven by market demand and national policies. However, long-term high-density farming in coastal waters has accelerated marine pollution, deteriorated water quality, and reduced the quality of aquatic products, thereby creating bottlenecks for nearshore cage aquaculture. In contrast, deep-sea cage aquaculture has attracted significant attention in China due to its advantages of high productivity, low environmental impact, and high-quality aquatic products. It is regarded as an important approach for structural adjustment in fisheries, facilitating the sustainable development of deep-sea aquaculture, alleviating nearshore aquaculture pressure, and reducing environmental pollution [1].

A deep-sea cage mainly consists of a float system, a netting system, a mooring system, and an operation platform. Among them, the netting system, being constantly immersed in seawater, provides a surface for algae, shellfish, and other organisms to attach and proliferate rapidly. This leads to mesh clogging, obstructs water exchange inside and outside the cage, and reduces dissolved

Preprints.org (www.preprints.org) | NOT PEER-REVIEWED | Posted: 22 October 2025 doi:10.20944/preprints202510.1743.v1

oxygen and food supply [2]. Therefore, the cleanliness of the netting is directly related to fish growth and survival rate [3].

Traditional cleaning methods often rely on high-pressure water jets and mechanical friction to remove biofouling. For instance, Zhang et al. [4] designed a manifold-type underwater high-pressure water jet cleaning machine that utilized cavitation jet impact to address net cleaning issues. Zhuang et al. [5] developed a swirling-type deep-sea net cleaning device integrated with underwater robots, where manifold-type rotating water jets served as the cleaning power source. A specially designed dual-float system adjusted underwater posture and direction, enabling cleaning in multiple orientations. Song et al. [6] developed a deep-sea cage net cleaning system composed of a surface workboat and an underwater cleaning device. The workboat was equipped with a small generator and crane, while rotary brushes performed intense frictional cleaning on the net surface to remove fouling organisms. Although high-pressure water jets offer high efficiency, their performance is limited by the pressure-bearing capacity of the netting. To overcome this limitation, the present study proposes incorporating abrasives into the jet, transforming cleaning from continuous water impact into particle cutting. This enables strong removal capability under low pressure [7]. Sheng et al. [8] experimentally compared the paint removal performance of low-pressure water jets with that of LPAWJ, confirming the superior effectiveness of the latter. The nozzle structure is a critical factor influencing the efficiency of abrasive water jets. Related studies have employed orthogonal experimental designs and RSM to optimize nozzle parameters and enhance cleaning performance [9]. Qiu et al. [10] utilized RSM combined with numerical simulation to optimize the high-pressure water jet parameters for cleaning deep-sea mining vehicles and identified the optimal combination for maximum impact performance. Wang et al. [11] applied orthogonal design to investigate the effects of key structural parameters on spray nozzle atomization and dust suppression performance, deriving the influence laws of nozzle design on efficiency. Sun et al. [12] studied a conventional Helmholtz nozzle by adding an expansion tube structure at the outlet to enhance cavitation effects, and numerically analyzed the effects of nozzle cavity height, cavity width, expansion angle, and pump pressure on cavitation jet performance. Previous studies have often focused on optimizing single indicators such as jet impact force, jet exit velocity, or jet flushing width, or conducted simultaneous optimization of multiple indicators [13]. However, these approaches either lacked comprehensiveness or required complex experimental setups. To balance efficiency and accuracy, this study introduces the entropy method to assign objective weights to multiple evaluation indicators, enabling a comprehensive assessment of cleaning performance across experimental conditions. The entropy method, known for its objectivity and adaptability, has been widely applied in environmental and enterprise performance evaluations [14].

In this paper, oysters were selected as the target fouling organisms. Using numerical simulation, the Box-Behnken design method, and the entropy method, the study investigates the influence of nozzle inlet pressure, nozzle outlet diameter, and target distance on the jet's overall removal capability, establishes a regression model, and determines the optimal parameter combination. The results provide theoretical guidance and optimization strategies for LPAWJ cleaning of cage nets.

2. Methods

2.1. CFD Method

FLUENT, as one of the most widely used commercial computational fluid dynamics(CFD) software packages internationally, offers significant advantages in simulating complex phenomena such as turbulence characteristics, multiphase flows, and transient dynamics. In this study, FLUENT is selected as the simulation tool to perform numerical analysis of the flow field resulting from the mixing of low-pressure water jets with abrasives for the removal of oyster biofouling on cage net.

 doi:10.20944/preprints202510.1743.v1

2.1.1. Geometric Model

Common nozzle types include cylindrical [15], fan-shaped [16], and custom-shaped designs [17]. In this study, based on the application of LPAWJ, a commercially available conical-straight nozzle was selected for modeling. To reduce the impact on the netting and meet environmental protection requirements, quartz sand was chosen as the abrasive, and a premixing method was employed to mix water and sand. As shown in Figure 1(a), the cleaning assembly consists of a water inlet interface, sand inlet interface, mixing chamber, and nozzle. High-pressure water enters the mixing chamber and creates a negative pressure that draws in the quartz sand. The water-abrasive mixture is then expelled through the nozzle to remove oyster fouling. The nozzle structure, shown in Figure 1(b), mainly comprises an inlet, contraction section, compression section, and outlet. Considering that the outlet diameter significantly affects abrasive velocity and jet impact force [18], it is selected as the key optimization parameter in this study. Other geometric parameters are kept constant: inlet diameter of 13.42 mm, contraction angle of 20°, compression section length of 24.8 mm, while the contraction section length is adjusted accordingly with the outlet diameter.

For numerical simulation, the flow field model of the nozzle was first constructed in *DesignModeler*, as shown in Figure 2. Based on statistical data, oysters were simplified as a cuboid measuring 60 × 40 × 3 mm. Simulation results show that abrasives maintain high velocity within 100-300 mm from the nozzle exit, forming an "abrasive velocity core" [19] that is crucial for effective fouling removal. Therefore, the target distance is set within the 100-300 mm range and is considered a key flow parameter. To prevent divergence in the flow field, the lateral width outside the nozzle is set to 20 mm, ensuring both energy efficiency and cleaning performance.

The geometric model was imported into *Meshing*, where the nozzle region was discretized using a sweep method to ensure vertical continuity. Due to the steep pressure gradients inside the nozzle, additional sweep partitions were introduced for local mesh refinement, enhancing the accuracy in capturing flow characteristics. The external flow field and oyster region were meshed using hexahedral elements. The final mesh configuration is shown in Figure 3.

Preprints.org (www.preprints.org) | NOT PEER-REVIEWED | Posted: 22 October 2025 doi:10.20944/preprints202510.1743.v1

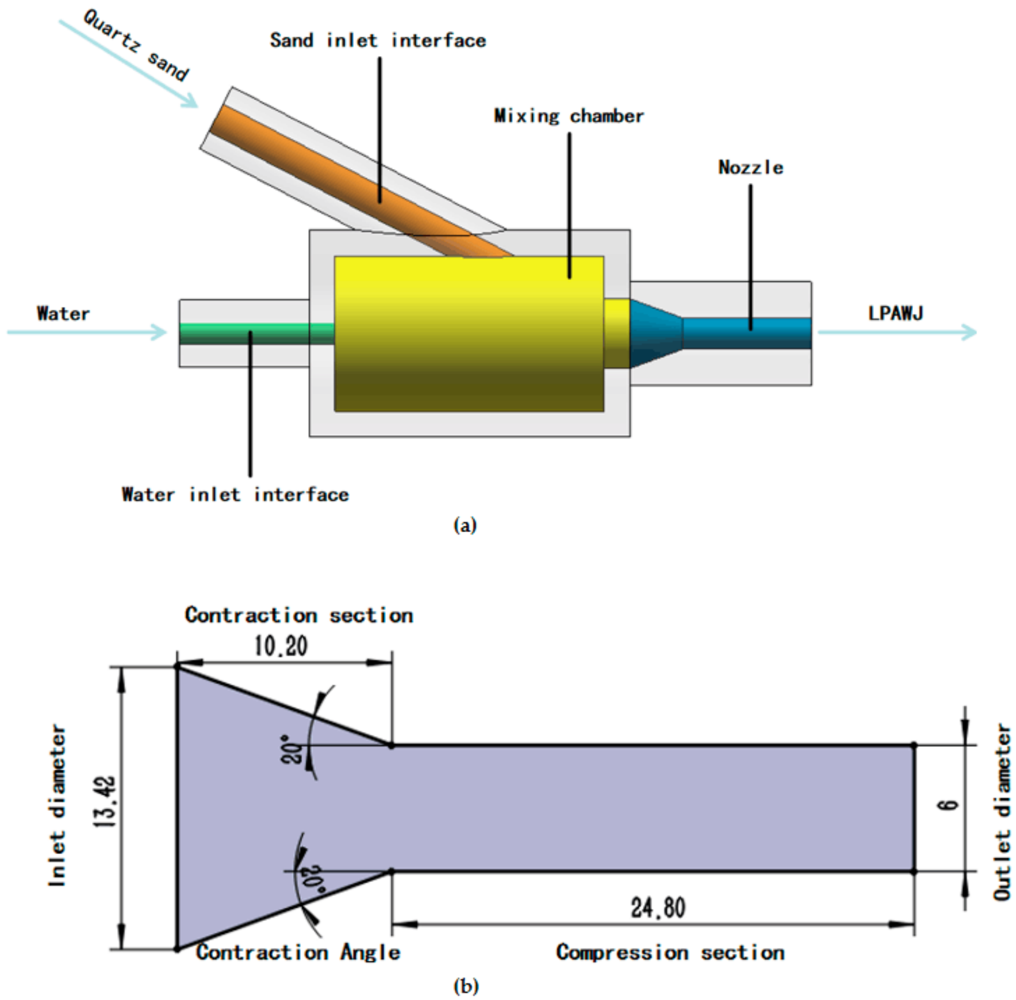

Figure 1. (a) Cleaning principle of low pressure quartz sand water jet; (b) Structure of nozzle.

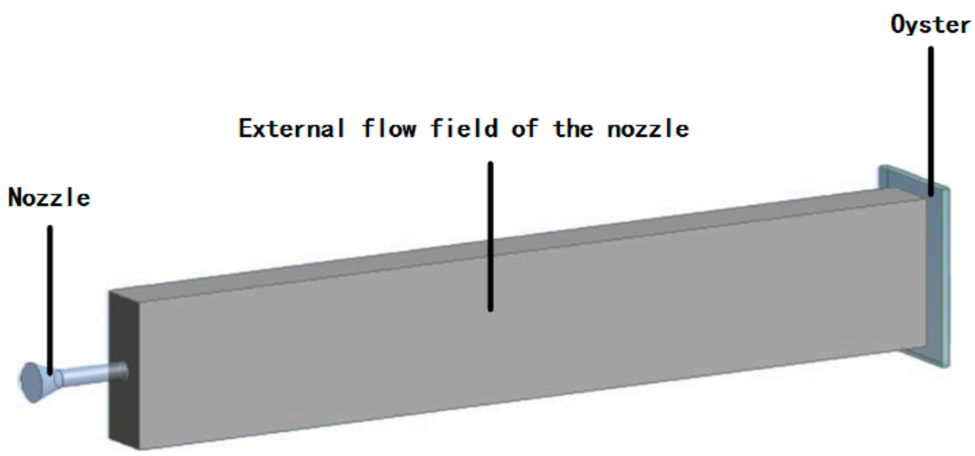

Figure 2. The Flow field model of the nozzle.

 doi:10.20944/preprints202510.1743.v1

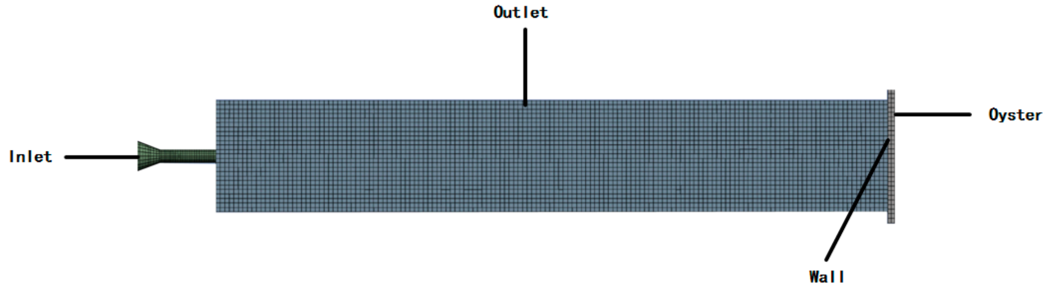

Figure 3. The meshing model of the whole simulation field.

2.1.2. Governing Equation

(1) Fluid Flow Equation

Water jets are treated as incompressible fluids, and the flow within the jet is governed by the continuity equation, momentum equation, and energy equation. The governing equations are as follows:

$$\frac{(1)\partial\rho_m}{\partial t}+\nabla\cdot(\rho_m\vec{v}_m)=0 \quad (1)$$

$$\frac{\partial}{\partial t}(\rho_m\vec{v}_m)+\nabla\cdot(\rho_m\vec{v}_m\vec{v}_m)=-\nabla p+\nabla\cdot[\mu_m(\nabla\vec{v}_m(2)+\vec{v}_m^T)] +\rho_m\vec{g}+\vec{F}+\nabla\cdot\left(\sum_{k=1}^{n}\alpha_k\rho_k\vec{v}_{dr,k}\vec{v}_{dr,k}\right) \quad (2)$$

where t is time, $\vec{v}_m$ is the velocity vector, p is the pressure acting on the fluid element, μ_m is the fluid viscosity, $\vec{F}$ is the body force, α_k is the volume fraction of the *k-th* phase, and $\vec{v}_{dr,k}$ represents the slip velocity between phases.

According to the Reynolds number estimated using the Reynolds formula, all three conical-straight nozzles used in this study exhibit Reynolds numbers greater than 2300 under various operating conditions, indicating fully developed turbulent flow. Therefore, the SST k-ε two-equation turbulence model is adopted to solve the high-Reynolds-number turbulent flow within the LPAWJ. The transport equations for turbulent kinetic energy k and specific dissipation rate ε are given as follows:

$$\frac{\partial}{\partial t}(\rho k)+\frac{\partial}{\partial X_i}((3)\rho k u_i)=\frac{\partial}{\partial X_j}\left[\left(\mu+\frac{\mu_t}{\sigma_k}\right)\frac{\partial k}{\partial X_j}\right]+G_k+G_b-\rho\varepsilon-Y_M+S_k \quad (3)$$

$$\frac{\partial}{\partial t}(\rho\varepsilon)+\frac{\partial}{\partial X_i}(\rho\varepsilon u_i)=\frac{\partial}{\partial X_j}\left[\left(\mu+\frac{\mu_t}{\sigma_\varepsilon}\right)\frac{\partial\varepsilon}{\partial X_j}\right]+(4)C_{1\varepsilon}\frac{\varepsilon}{k}(G_k+C_{2\varepsilon}c_B)-c_{2\varepsilon}\rho\frac{\varepsilon^2}{k}+S_\varepsilon \quad (4)$$

where G_k is the production of turbulent kinetic energy due to mean velocity gradients, G_b is the production due to buoyancy, and Y_M accounts for the dilatation dissipation. and ε denote turbulent kinetic energy and specific dissipation rate, respectively, $\sigma_k$and σ_ε are turbulent Prandtl numbers for k and ε. The turbulent viscosity is calculated as:

$$(5)\ \mu_t=\rho C_\mu\frac{k^2}{\varepsilon} \quad (5)$$

In the numerical simulation using FLUENT, the empirical constants are set as follows, C_μ=0.9, σ_k=1.0, σ_ε=1.3 [20].

(2) Particle trajectory calculation equation

In FLUENT, when the volume fraction of solid particles in the flow within is less than 10%, the Discrete Phase Model (DPM) is typically used for simulation [21]. Given that the volume fraction of quartz sand abrasives in this study is relatively low, the quartz sand particles are treated as a discrete phase, and the DPM is employed to calculate their transport trajectories.

In this study, additional forces acting on abrasive particles are neglected. Under a Cartesian coordinate system, the force balance equation for a single abrasive particle can be expressed as:

$$(6)\ \frac{du_p}{dt}=F_D(u_f-u_p)+\frac{g(\rho_p-\rho_f)}{\rho_p} \quad (6)$$

 doi:10.20944/preprints202510.1743.v1

where u_p and ρ_p represent the velocity and density of the particle, respectively; $F_D(u_f\text{-}u_p)$ is the drag force; and $\frac{g(\rho_p\text{-}\rho_f)}{\rho_p}$ is the gravitational force. The expression for the drag force F_D is given by:

$$(7)\quad F_D = \frac{18\mu}{\rho_p d_p^2}\frac{C_D Re}{24}\quad (7)$$

where d_p is the particle diameter, C_D is the drag coefficient, and Re is the Reynolds number of the fluid flow around the particle.

2.1.3. Boundary Conditions and Solution Settings

To improve the accuracy of the numerical simulation, appropriate boundary conditions were defined in this study. The nozzle inlet was set as a pressure inlet, the outlet as a pressure outlet, and all other surfaces were defined as no-slip adiabatic walls. The nozzle outlet pressure was fixed at 101,325 Pa. According to Bernoulli's principle, the inlet pressure directly affects the jet exit velocity, which in turn influences the effectiveness of fouling removal. Therefore, inlet pressure was selected as a key parameter. Quartz sand particles were modeled as rigid spheres of uniform size, with detailed parameters listed in Table 1. At wall boundaries, particles were assigned the "Reflect" condition, resulting in perfectly elastic collisions with the surface. At the outlet, the "Escape" condition was applied, allowing particles to exit the flow within [22].

Table 1. Parameters of quartz sand particles.

Particle density(kg/m³)	Particle size(mm)	Particle mass flow rate(kg/s)
2600	0.6	0.075

Since the oyster removal process by LPAWJ involves both water and air phases, the Volume of Fluid (VOF) model with transient tracking capability was employed [23], with the two phases set as immiscible. To enhance pressure calculation accuracy, the Pressure-Implicit with Splitting of Operators(PISO) algorithm was used for transient solution [24].

To validate the simulation results, a comparison was made between the theoretical and simulated jet velocities at the nozzle inlet under different inlet pressures. Based on Bernoulli's principle, the relationship between jet velocity and inlet pressure can be simplified as:

$$(8)\, v = \sqrt{\frac{2P}{\rho}}\quad (8)$$

where v is the water jet velocity at the nozzle inlet, P is the inlet pressure, and ρ is the water density.

A comparison of the theoretical and simulated inlet jet velocities is shown in Table 2. The results indicate that the error between the simulated and theoretical velocities ranges from 0.095% to 0.01%, demonstrating strong agreement and confirming the high accuracy of the numerical simulation.

Table 2. Comparison of theoretical and simulated water jet velocities at the nozzle inlet.

Inlet pressure (MPa)	Theoretical water jet velocity (m/s)	Simulated water jet velocity (m/s)	Error
2.5	70.70	70.77	0.099%
3.5	83.66	83.74	0.096%
4.5	94.86	94.95	0.095%

2.1.4. Mesh Independence Verification

Generally, mesh size has a significant impact on the accuracy of flow within calculations [25]. In this study, four meshing schemes were developed by adjusting the mesh size under the conditions of a nozzle inlet pressure of 3.5 MPa, nozzle outlet diameter of 6 mm, particle mass flow rate of 0.1 kg/s, and target distance of 100 mm. As shown in Table 3, the evaluation indicators used include the

 doi:10.20944/preprints202510.1743.v1

fluid outlet velocity and the peak jet impact force. The simulation results from schemes W_1 to W_4 indicate that when the mesh count is 15,446 (W_1), the resolution is too coarse, leading to significant computational deviation. When the mesh count exceeds 22,886, the variations in both evaluation indicators become relatively small. Considering both computational accuracy and efficiency, mesh scheme W_3 was selected as the optimal configuration for this study.

Table 3. Mesh independence verification.

Solution	W_1	W_2	W_3	W_4
Mesh cell	15446	19327	22886	27116
Fluid outlet velocity (m/s)	60.2416	76.6049	76.5060	76.5367
Peak jet impact force (Pa)	3623266	4145702	4197250	4119664

2.2. Multi-Parameter Optimization Design Method

The Box-Behnken design is an advanced statistical experimental design method within the framework of RSM, capable of systematically evaluating the effects of multiple independent variables and their interactions on a response variable [26]. Compared to full factorial designs, the Box-Behnken approach requires fewer experimental runs, thereby saving time and resources. Moreover, it avoids extreme parameter combinations, which helps prevent divergence in simulations. Therefore, the Box-Behnken design was employed to investigate the fouling removal characteristics of LPAWJ for cage net cleaning.

2.2.1. Selection of Optimization Parameters

The optimization parameters in this study include nozzle inlet pressure X_1, nozzle outlet diameter X_2, and target distance X_3. While the parameter ranges for X_2 and X_3 have been analyzed in the preceding sections, determining the appropriate range for the nozzle inlet pressure X_1 is particularly critical.

Numerical simulations were performed on the flow field of LPAWJ removing oysters attached to cage nets. Effective detachment occurs when the jet impact force exceeds the compressive strength of the oyster shell. Therefore, it is essential to first determine the compressive limit of the oyster shell. Due to the lack of relevant data in existing literature, compression tests were conducted using a tensile-compression testing machine on 20 oysters of varying shapes, focusing on the thickest part of each shell. The experimental setup for the oyster compression test is illustrated in Figure 4. The initial failure loads were recorded, and the average critical compressive load was calculated to be 228 N, as shown in Figure 5. By uniformly applying ink to the contact surface of the indenter, the contact area between the indenter and oyster shell was determined to be approximately 7.6×10^{-5} m². This leads to an estimated compressive strength of the oyster shell of about 3 MPa. Based on this compressive strength and the previously determined ranges for X_2 and X_3, the suitable range for nozzle inlet pressure X_1 was established through numerical simulations. The experimental ranges and levels for all optimization parameters are presented in Table 4.

Preprints.org (www.preprints.org) | NOT PEER-REVIEWED | Posted: 22 October 2025 doi:10.20944/preprints202510.1743.v1

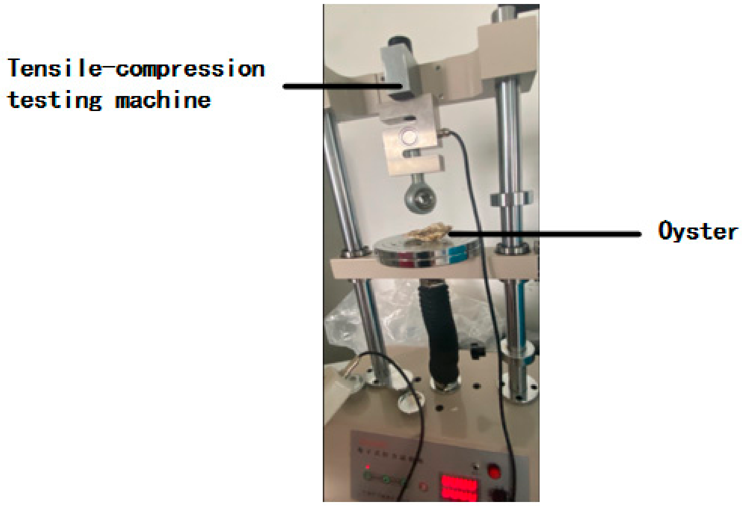

Figure 4. Oyster ultimate pressure test.

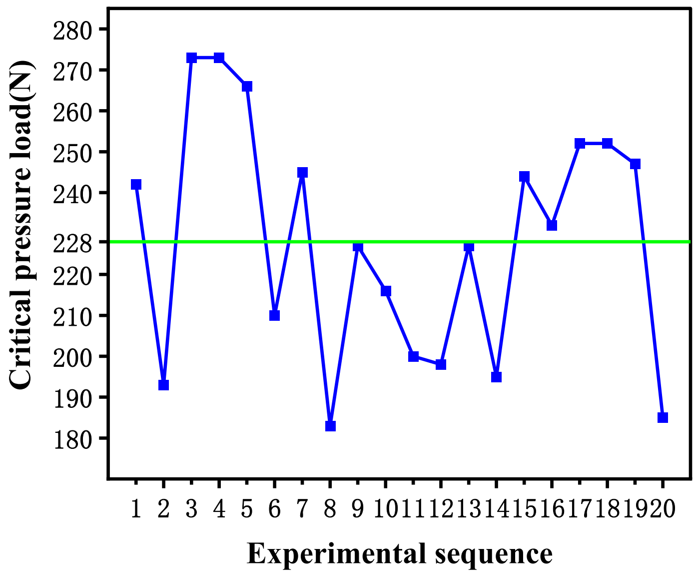

Figure 5. Oyster ultimate pressure test.

Table 4. Response surface experiment parameter levels.

Optimization Parameter	Parameter Code	Unit	Lower Level(-1)	Zero Level(0)	Upper Level(1)
Nozzle inlet pressure	X_1	MPa	2.5	3.5	4.5
Nozzle outlet diameter	X_2	mm	6	8	10
Target distance	X_3	mm	100	200	300

2.2.2. Selection of Target Response

In multi-scheme evaluations, multi-criteria decision-making methods play a crucial role in enabling scientifically grounded decisions. Among these, the entropy method is a widely adopted objective weighting approach, frequently used for comprehensive assessments. Its procedure involves data normalization, calculation of information entropy, determination of the divergence coefficient, computation of weights, and ultimately, the calculation of a comprehensive score [27]. Its procedure includes data standardization, calculation of information entropy, difference coefficients, weights, and comprehensive scores. In this study, the removal capability of LPAWJ was characterized by four indicators: peak jet impact force Z_1, stable jet impact force Z_2, peak abrasive-water jet velocity Z_3, and peak abrasive particle velocity Z_4. Z_1 reflects whether the jet can achieve fouling removal, while Z_2 represents the jet's sustained removal performance. Both Z_1 and Z_3 are positively correlated, and Z_4 determines the abrasive particle's impact effect and the associated rebound phenomenon upon contacting the fouling surface. Rebound effects alter the velocity distribution and impact frequency of subsequent particles, thereby influencing removal efficiency. Consequently, these four indicators were selected as evaluation metrics for the jet's overall removal capability. Based on the results of the Box-Behnken design simulations, the weights of each indicator were determined using the entropy method, and a comprehensive score Y for each experimental point-representing the jet's overall removal capability-was calculated. The computational process of the entropy method is illustrated in Figure 6.

After defining the optimization parameters and response objective, a total of 17 sets of numerical simulation experiments (including 5 center points) were designed using the coded values from Table 4. Each simulation was repeated three times, and the average values of the four evaluation indicators were obtained using FLUENT. The results are presented in Table 5. These indicator data were uploaded to the SPASSAU platform, where the entropy method was used to compute the weighting coefficients, as shown in Table 6. Results showed that the contribution order of the indicators to the jet's overall removal capability was $Z_2 > Z_1 > Z_3 > Z_4$. Using the derived weights, the jet's overall removal capability for each experimental point was calculated, with the results also listed in Table 5. Subsequently, Design-Expert software was employed to analyze the experimental results, and a response surface model was constructed using the least-squares method [28], with the following expression:

$$(9)Y=\beta_0+\sum_{i=1}^{k}\beta_i X_i+\sum_{i=1}^{k}\beta_{ii} X_i^2+\sum_{i,j}^{k}\beta_{i,j} X_i X_j \quad i<j \quad (9)$$

In the model expression, Y represents the response variable (target response), X denotes the optimization parameters, are the coefficients of the linear terms, β_i is the slope of parameter X_i, is the quadratic term of parameter X_i, and $\beta_{i,j}$ are the coefficients of the interaction terms between parameters X_i and X_j.

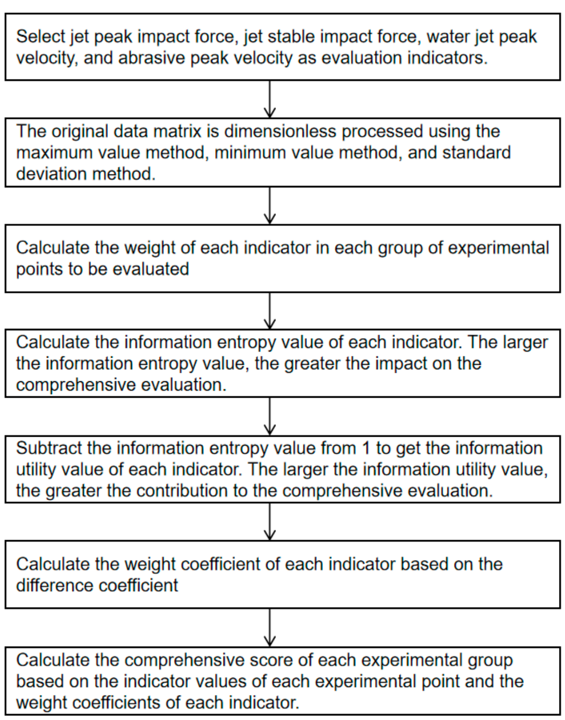

.

 doi:10.20944/preprints202510.1743.v1

Figure 6. The process of calculating the comprehensive score of each group of experimental points using the entropy method.

Table 5. Experimental results.

Run	X_1(MPa)	X_2(mm)	X_3(mm)	Z_1(Pa)	Z_2(Pa)	Z_3(m/s)	Z_4(m/s)	Y
1	3.5	8	200	3772636	2563217	83.436	83.873	2131847
2	3.5	8	200	3807649	2421355	83.400	83.815	2092102
3	2.5	8	300	2791840	2438962	80.937	80.836	1772445
4	3.5	10	100	3487516	2650094	83.885	82.853	2071570
5	4.5	6	200	5034319	2574198	90.678	88.586	2622321
6	4.5	10	200	5950920	4146674	97.620	95.164	3399931
7	3.5	6	300	4073072	3795392	105.510	78.577	2671069
8	3.5	8	200	3810632	2436794	83.396	83.815	2098607
9	3.5	8	200	3810632	2436794	83.396	83.815	2098607
10	4.5	8	100	4491512	3341128	93.687	91.643	2642102
11	3.5	6	100	3659127	2079154	79.694	78.368	1921461
12	2.5	10	200	3300805	2412436	74.987	73.879	1926242
13	3.5	8	200	3810632	2436794	83.396	83.815	2098607
14	3.5	10	300	4281541	3139775	87.091	86.871	2502358
15	2.5	8	100	2870546	2135317	69.499	68.141	1688578
16	2.5	6	200	3938491	2561902	94.761	84.247	2184601
17	4.5	8	300	5158842	3993358	108. 082	107.420	3090652

Table 6. Weight coefficients of evaluation index values.

Item	Information entropy value	Information utility value	Weight coefficient
eZ_1(Pa)	0.888	0.112	32.091
Z_2(Pa)	0.875	0.125	35.937
Z_3(m/s)	0.94	0.06	17.145
Z_4(m/s)	0.948	0.052	14.828

3. Results and Discussion

3.1. Regression Equation

Using Design-Expert software to perform multiple regression analysis, the polynomial regression model between the three optimization parameters and the response was obtained as follows:

$$Y=8421040-2088820X_1-1208700X_2+8930.94X_3+30489.88X_1X_2+911.59X_1X_3-539.53X_2X_3+331175X_1^2+74039.25X_2^2-13.67X_3^2 \quad (10)$$

3.2. Analysis of variance (ANOVA)

Table 7 presents the ANOVA results for the regression model, which examines the relationship between the three optimization parameters and the jet's overall removal capability. The *p*-value is used to assess statistical significance, where $p < 0.01$ indicates a highly significant effect, and $p < 0.05$ indicates a significant effect [29]. The results show that the overall model has a *p*-value less than 0.0001, indicating that the response surface model is highly significant. In terms of individual factor effects, both X_1 (nozzle inlet pressure) and X_3 (target distance) have *p*-value below 0.0001, demonstrating extremely significant influence. X_2 (nozzle outlet diameter) has a *p*-value of 0.0191, indicating a relatively smaller but still significant effect. Based on the *f*-value, the factors' influence on the response follows the order: $X_1 > X_3 > X_2$. Regarding two-factor interactions, the *p*-value for $X_1 \times X_3$ and $X_2 \times X_3$ are 0.0062 and 0.0026, respectively, indicating significant interaction effects. The interaction between X_1 and X_2 also shows a significant effect with a *p*-value of 0.0362, though it is comparatively weaker.

Table 7. ANOVA for regression models.

Source	Sum of Squares	df	Mean Squares	*F-Value*	*P-Value*
Model	4.912E+12	9	5.458E+11	245.36	< 0.0001
X_1	3.439E+12	1	3.439E+12	1545.99	< 0.0001
X_2	2.042E+10	1	2.042E+10	9.18	0.0191
X_3	4.371E+11	1	4.371E+11	196.49	< 0.0001
X_1X_2	1.487E+10	1	1.487E+10	6.69	0.0362
X_1X_3	3.324E+10	1	3.324E+10	14.94	0.0062
X_2X_3	4.657E+10	1	4.657E+10	20.94	0.0026
X_1^2	4.618E+11	1	4.618E+11	207.61	< 0.0001
X_2^2	3.693E+11	1	3.693E+11	166.02	< 0.0001
X_3^2	7.868E+10	1	7.868E+10	35.37	0.0006
Residual	1.557E+10	7	2.224E+09		
Lack of Fit	1.457E+10	3	4.856E+09		
Pure Error	0	4	0		
Cor. Total	4.928E+12	16			

The quality of the regression model was further evaluated using the coefficient of determination (R^2), adjusted R^2 ($Adj\ R^2$), predicted R^2 ($Pred\ R^2$), adequate precision (Adeq Precision), and coefficient of variation (*C.V*) [30], as shown in Table 8 . The results indicate that R^2, $Adj\ R^2$, and $Pred\ R^2$ are 0.9968, 0.9928, and 0.9524, respectively,all close to 1. The difference between $Adj\ R^2$ and $Pred\ R^2$ is less than 0.2, confirming the model's strong fit and coefficient reliability. The Adeq Precision is 52.447, far exceeding the threshold of 4, while the *C.V* is 2.02%, well below 10%, indicating low variability in prediction error [31]. In summary, the regression model demonstrated high reliability in predicting jet's overall removal capability under varying conditions.

Table 8. Evaluation results of the regression model.

R^2	*Adj* R^2	*Pred* R^2	Adeq Precision	*C.V*
0.9968	0.9928	0.9524	52.447	2.02%

3.3. Single Parameter Analysis

This section analyzes the relationship between the three optimization parameters and the jet's overall removal capability. As shown in Figure 7(a), the removal capability increases in a near-parabolic trend with rising nozzle inlet pressure, with a notably accelerated growth observed beyond 3.5 MPa. Figure 7(b) illustrates that as the nozzle outlet diameter increases, the removal performance initially decreases and then increases. Figure 7(c) indicates that the removal capability improves with increasing target distance; however, the rate of improvement slows beyond 200 mm and shows a declining trend when approaching or exceeding 300 mm.

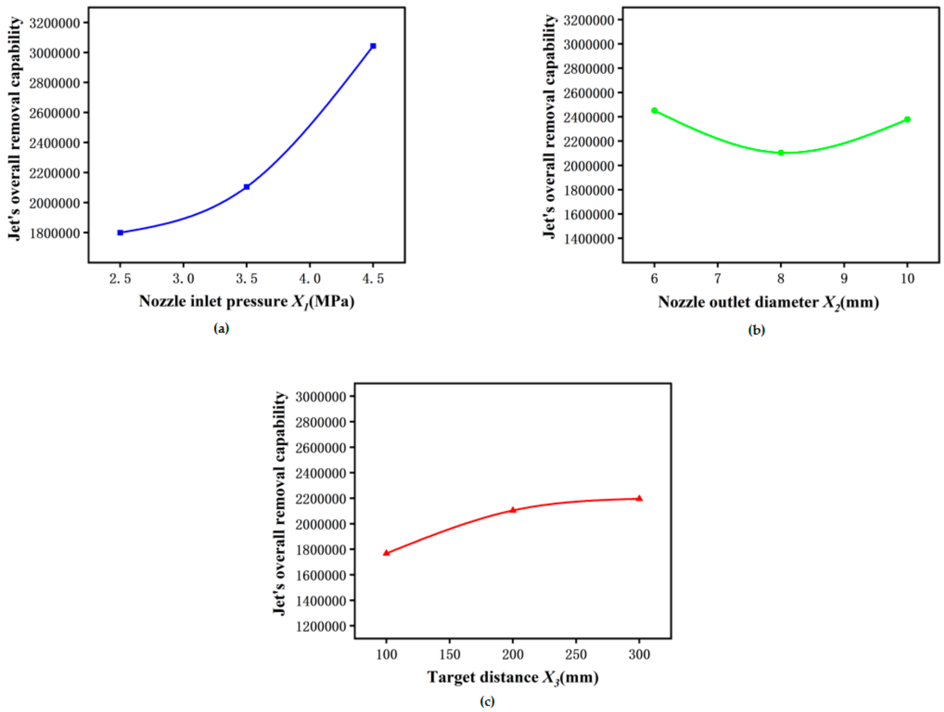

Figure 7. (a) Relationship between jet's overall removal capability and nozzle inlet pressure; (b) Relationship between jet's overall removal capability and outlet diameter; (c) Relationship between jet's overall removal capability and target distance.

3.4. Two-Parameter Analysis

This section analyzes the interactive effects of three parameter combinations on the jet's overall removal capability. As shown in Figure 8, the combination of nozzle inlet pressure and outlet diameter achieves a peak removal capacity of 3,377,709 when X_1 = 4.5 MPa and X_2 = 10 mm. When the inlet pressure is held constant, the removal capability first decreases and then increases with the outlet diameter. Conversely, with a fixed outlet diameter, the removal capacity increases significantly with the inlet pressure, indicating that inlet pressure has a greater influence. The presence of both circular and elliptical contour lines in the figure suggests that the interaction between the two parameters is not significant [32].

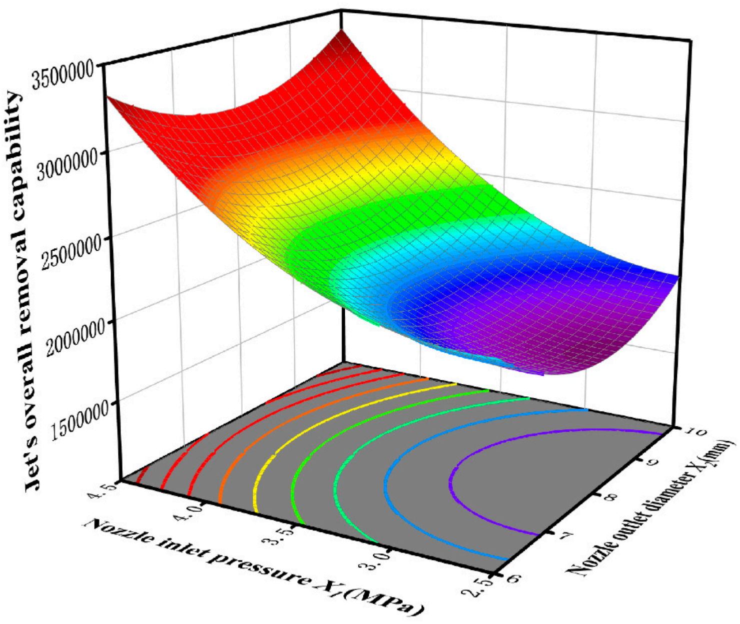

Figure 8. Effect of the interaction between nozzle inlet pressure and nozzle outlet diameter on the comprehensive stripping ability of the jet(X_3 = 200mm).

Figure 9. illustrates the interactive effect between nozzle inlet pressure and target distance on the jet's overall removal capability. The peak value occurs at X_1 = 4.5 MPa and X_3 = 300 mm, corresponding to a removal capacity of 3,225,590. Using the same analytical approach, it is evident that both parameters have significant effects, with inlet pressure exerting a stronger influence. Compared to the first parameter combination, the response surface in this case exhibits a steeper slope and greater gradient, with elliptical contour lines, indicating a more pronounced interaction between the two parameters and a stronger overall effect.

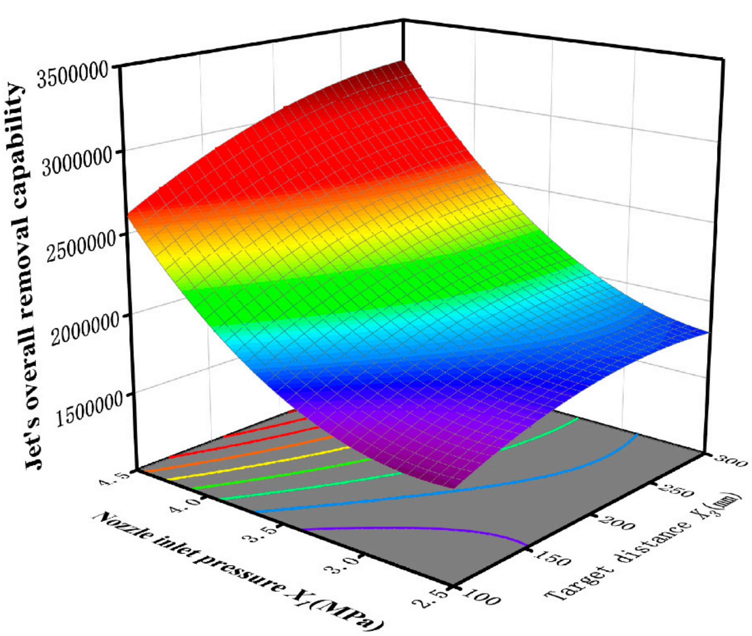

Preprints.org (www.preprints.org) | NOT PEER-REVIEWED | Posted: 22 October 2025 doi:10.20944/preprints202510.1743.v1

Figure 9. Effect of the interaction between nozzle inlet pressure and target distance on the comprehensive stripping ability of the jet(X_2 = 8mm).

Figure 10. illustrates the interactive effect of nozzle outlet diameter and target distance on the jet's overall removal capability. The peak value is observed at X_2 = 6 mm and X_3 = 300 mm, with a corresponding removal capacity of 2,621,828. Using the same analytical method, it can be concluded that both parameters have significant effects, with target distance exerting a stronger influence. Compared to the second parameter combination, this response surface exhibits a lower slope and gentler gradient; however, the presence of elliptical contour lines indicates that the interaction between these two parameters remains significant.

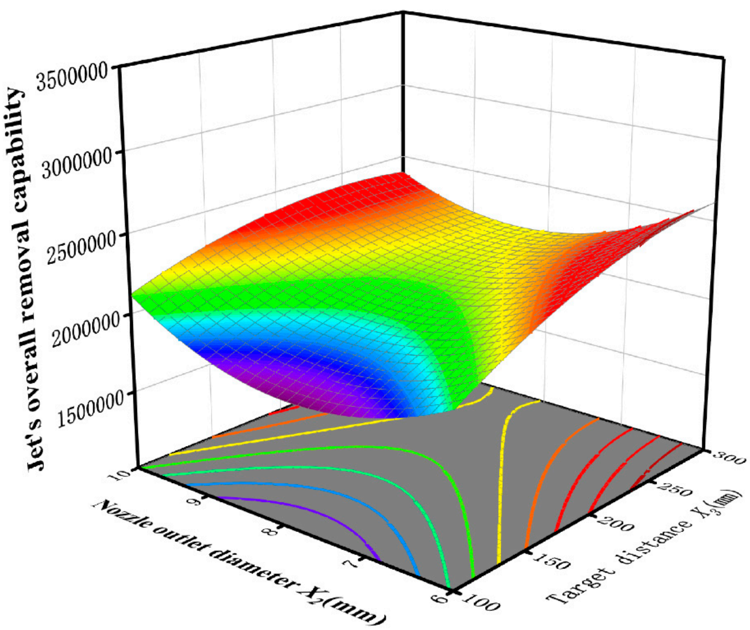

Figure 10. Effect of the interaction between nozzle outlet diameter and target distance on the comprehensive stripping ability of the jet(X_1 = 3.5MPa).

3.5. Multi-Parameter Optimization Design and Optimization Results

After establishing the polynomial regression model describing the relationship between the three optimization parameters and the jet's overall removal capability, the Design-Expert software was used to maximize the objective function. The goal was to identify the optimal combination of parameters-within the defined experimental range-that yields the highest jet's overall removal capability based on the regression model:

FindMax$Y=[X_1,X_2,X_3]^T$(2.5MPa<X_1<4.5MPa,6mm<X_2<10mm,100mm<X_3<300mm)

As shown in Table 5, experimental point 15 resulted in the lowest removal capability, with both the peak jet impact force Z_1 and the stable jet impact force Z_2 being insufficient to remove oysters. This condition is referred to as Condition 1 in this study. In contrast, experimental point 5 achieved the highest removal capability and is designated as Condition 2. By solving the regression model, the optimal parameter combination was determined to be: nozzle inlet pressure X_1 = 4.5 MPa, nozzle outlet diameter X_2 = 10 mm, and target distance X_3 = 205.396 mm. This optimal condition is referred to as Condition 3, with a predicted maximum jet's overall removal capability of 3,408,646. A numerical simulation was conducted using this optimized parameter set to obtain the actual values of the evaluation indicators, from which the actual jet's overall removal capability was calculated, as shown in Table 9. The deviation between the predicted and actual values was only 1.89%, indicating a high level of reliability in the optimization results.

Table 9. Comparison of simulation results and optimization results under Condition 3.

Z_1(Pa)	Z_2(Pa)	Z_3(m/s)	Z_4(m/s)	Actual *Y* value	Predicted *Y* value
6313952	4029857	93.9754	93.6029	3474450	3408646

Figure 11 compares the velocity and pressure contour plots for the three operating conditions. It is evident that the trends of velocity and pressure variations of the abrasive water jet are largely consistent across different conditions. Before reaching the oyster surface, the abrasive jet maintains a relatively high velocity and low pressure. Upon impact with the oyster surface, the pressure rises sharply, generating a substantial jet impact force that facilitates the fragmentation and removal of the oysters. Simultaneously, both the water jet and abrasive particles experience rebound and splashing, resulting in a subsequent reduction in velocity.

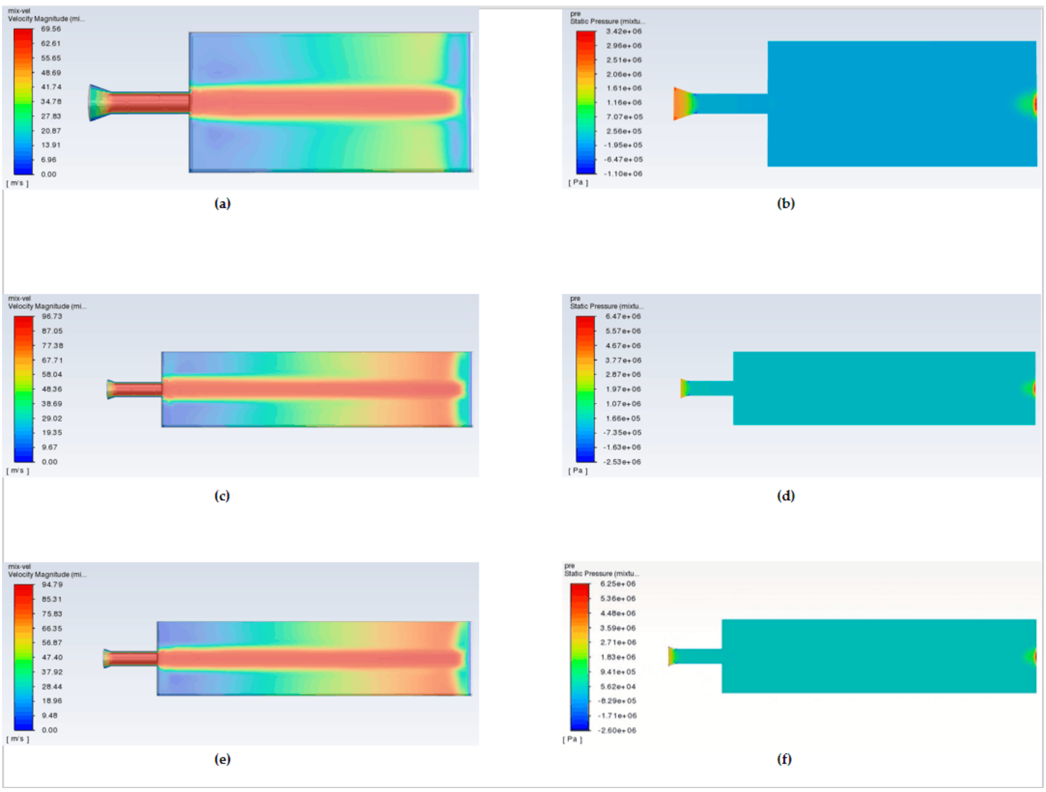

Figure 11. (a) Speed cloud diagram of operating condition 1; (b) Pressure cloud diagram of operating condition 1; (c) Speed cloud diagram of operating condition 2; (d) Pressure cloud diagram of operating condition 2; (e) Speed cloud diagram of operating condition 3; (f) Pressure cloud diagram of operating condition 3.

Figure 12 compares the axial abrasive water jet velocity, axial abrasive particle velocity, and jet impact force under the three working conditions. From Figures 12(a), 12(b), and 11, the abrasive water jet and abrasive particle velocities in Conditions 2 and 3 are significantly higher than those in Condition 1, with peak velocities occurring near the oyster surface. Specifically, the peak abrasive water jet velocities in Conditions 2 and 3 increase by 40.46% and 35.22%, respectively, compared to Condition 1, while the peak abrasive particle velocities rise by 39.66% and 37.37%. These increases are attributed to the higher nozzle inlet pressure, which provides greater kinetic energy to the water jet. This energy enhances the entrainment and acceleration of abrasive particles, enabling more effective removal upon contact with the oyster surface. Figure 12(c) shows that the peak jet impact forces in Conditions 2 and 3 rise by 107.31% and 119.96%, respectively, relative to Condition 1, while their stable impact forces increase by 94.19% and 88.72%. Despite Conditions 2 and 3 sharing identical inlet pressure X_1 and nozzle diameter X_2, the peak jet and abrasive velocities in Condition 2 are slightly higher. However, its impact force is lower than that of Condition 3. This is explained by Figure 13: at a target distance of 200 mm (Condition 2), the abrasive particles have not yet reached the oyster surface when the water jet makes initial contact. In contrast, at 205.396 mm (Condition 3), the slightly reduced jet velocity is offset by the simultaneous impact of both water and abrasives. The synchronized action produces a stronger peak impact force, enhancing the overall removal capability. Indeed, the jet's overall removal capability in Condition 3 is 2.19% higher than in Condition 2, underscoring the superiority of the optimized parameter set in Condition 3.

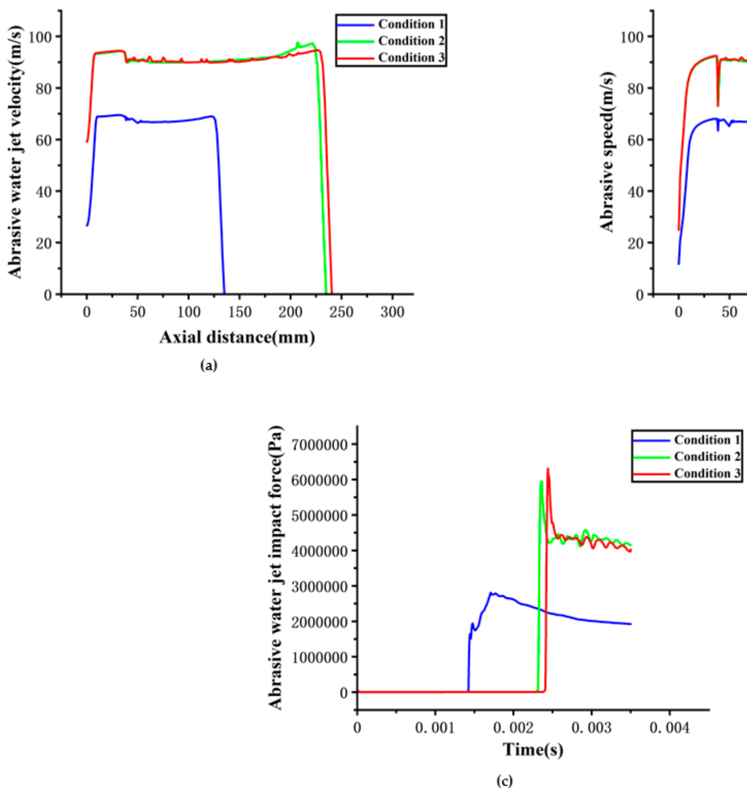

Figure 12. (a) The speed distribution of abrasive water jet along the axis under 3 working conditions; (b) The speed distribution of abrasive along the axis under 3 working conditions; (c) The impact force of abrasive water jet under 3 working conditions.

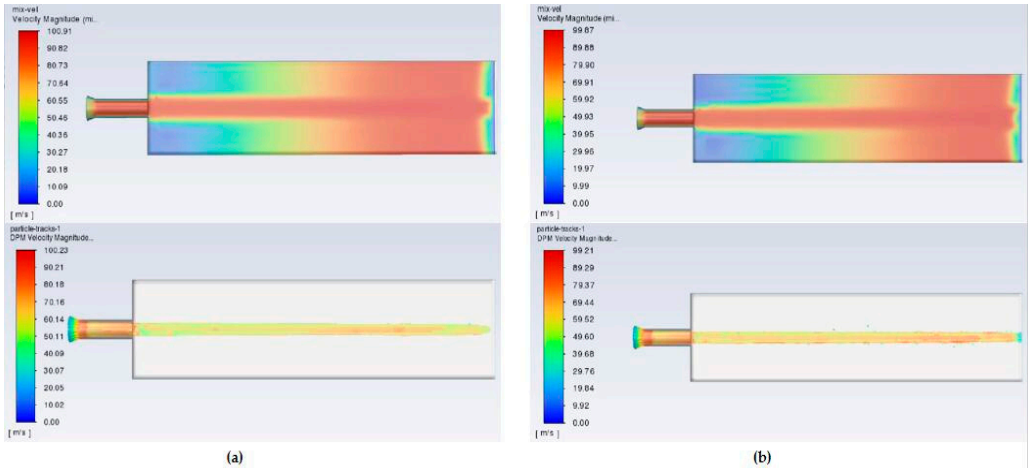

Figure 13. (a) Abrasive trajectory diagram of working conditions 2 when the water jet just contacts the oyster surface; (b) Abrasive trajectory diagram of working conditions 3 when the water jet just contacts the oyster surface.

4. Conclusions

This study integrates numerical simulation, the Box-Behnken response surface method, and the entropy method to analyze the effects of nozzle inlet pressure, nozzle outlet diameter, and target distance on the jet's overall removal capability. A regression model was established, and the optimal parameter combination was determined. The main conclusions are as follows:

(1)Evaluation Indicators and Weighting: Four indicators were selected to evaluate the jet's overall removal capability: peak jet impact force Z_1, stable jet impact force Z_2, peak abrasive-water jet velocity Z_3, and peak abrasive particle velocity Z_4. Using the entropy method, the weights of these indicators were determined. Results showed that their contributions to removal capability ranked as follows: $Z_2 > Z_1 > Z_3 > Z_4$.

(2)Significance Analysis: Analysis of variance and parameter analysis revealed that all three optimization parameters significantly influenced the jet's overall removal capability. The order of influence was: nozzle inlet pressure > target distance > nozzle outlet diameter. Furthermore, significant interaction effects were observed between parameters, particularly between nozzle inlet pressure and target distance, and between nozzle outlet diameter and target distance.

(3)Optimization Results: Optimization based on the response surface regression model yielded the optimal parameter combination: nozzle inlet pressure X_1 = 4.5 MPa, nozzle outlet diameter X_2 = 10 mm, and target distance X_3 = 205.396 mm. Under this configuration, the water jet and abrasive particles simultaneously impact the oyster surface, increasing the peak jet impact force. As a result, the jet's overall removal capability was improved by 2.19% compared to the parameter set used in Condition 2.

Author Contributions: Writing—original draft preparation, Y.W.; Software, Y.W.; Writing–review and editing, Y.T.; Investigation, B.D. and G.X.; Formal analysis, H.L.; Methodology, H.C. All authors have read and agreed to the published version of the manuscript.

Funding: This research received no external funding.

Institutional Review Board Statement: Not applicable.

Informed Consent Statement: Not applicable.

Data Availability Statement: The data presented in this study are available on request from the correonding author

Conflicts of Interest: The authors declare no conflicts of interest.

References

1. Huang, X., et al., Review of Engineering and Equipment Technologies for Deep-Sea Cage Aquaculture in China Progress in Fishery Sciences, 2022. 43(06): p. 121–131.
2. Song, X., et al., Research progress of deep－water cage cleaning technology and devices. Fishery Modernization, 2021. 48(5): p. 1–9.
3. Frazer, L.N., Sea-cage aquaculture, sea lice, and declines of wild fish. Conserv Biol, 2009. 23(3): p. 599–607.
4. Zhang, X., et al., Design of high-pressure water-jet manifold underwater net-washing machine. South China Fisheries Science, 2010. 6(3): p. 46–51.
5. Zhuang, J., et al., Design of a New Deep-sea Net Cage Cleaning Robot. Machinery, 2018. 45(01): p. 72–75.
6. Song, Y. and X. Zheng, Design and study of the clean equipments of deep－sea net cage. Mechanical Research & Application, 2012. 25(02): p. 41–43+46.
7. Li, J.-B., et al., The flow field characteristics and rock breaking ability of cone-straight abrasive jet, rotary abrasive jet, and straight-rotating mixed abrasive jet. Petroleum Science, 2025. 22(6): p. 2457–2464.
8. Xiong, S., et al., Parameter Optimization and Effect Analysis of Low-Pressure Abrasive Water Jet (LPAWJ) for Paint Removal of Remanufacturing Cleaning. Sustainability, 2021. 13(5).
9. Qiu, Y., et al., Optimization design of nozzle parameters under the condition of submerged water jet breaking soil based on response surface method. Applied Ocean Research, 2025. 154.
10. Qiu, X., et al., A Study on the Optimization of Water Jet Decontamination Performance Parameters Based on the Response Surface Method. Applied Sciences, 2024. 14(16).
11. Wang, P., et al., Structural parameters optimization of internal mixing air atomizing nozzle based on orthogonal experiment. Coal Science and Technology, 2023. 51(09): p. 129–139.
12. Sun, P., et al., Parametric Study on Self-excited Vibration Cavitation Jet Nozzles based on the CFD Method. Fluid Machinery, 2019. 47(10): p. 1–7+19.
13. Liu, Y., et al., Structural optimization design of ice abrasive water jet nozzle based on multi-objective algorithm. Flow Measurement and Instrumentation, 2024. 97.
14. Wang, B., et al., Development of a comprehensive pollution evaluation system based on entropy weight-fuzzy evaluation model for urban rivers: A case study in North China. Journal of Water Process Engineering, 2024. 67.
15. Hu, K., Z. Ai, and J. Yu, Study for Cylindrical Nozzle Structure Optimization Based on Response Surface Method. Machine Tool & Hydraulics, 2014. 42(01): p. 27–30.
16. Lin, X., et al., Study of Low-pressure Jet Characteristic of Fan Nozzle. Machine Tool & Hydraulics, 2015. 43(03): p. 164–167.
17. Lai, Y., et al., Experimental Study on the Jet Characteristic of Non-circle Jet Nozzle. Light Industry Machinery, 2005(04): p. 23–25.
18. Zhong, L., et al., Simulation analysis and evaluation of decontamination effect of different abrasive jet process parameters on radioactively contaminated metal. Nuclear Engineering and Technology, 2023. 55(11): p. 3940–3955.
19. Cai, C., et al., Particle velocity distributions of abrasive liquid nitrogen jet and parametric sensitivity analysis. Journal of Natural Gas Science and Engineering, 2015. 27: p. 1657–1666.
20. López, A., et al., CFD study of Jet Impingement Test erosion using Ansys Fluent® and OpenFOAM®. Computer Physics Communications, 2015. 197: p. 88–95.
21. Cheng, W., et al., Investigation on wear induced by solid-liquid two-phase flow in a centrifugal pump based on EDEM-Fluent coupling method. Flow Measurement and Instrumentation, 2024. 96.
22. Jerman, M., H. Orbanić, and J. Valentinčič, CFD analysis of thermal fields for ice abrasive water jet. International Journal of Mechanical Sciences, 2022. 220.
23. Garoosi, F. and K. Hooman, Numerical simulation of multiphase flows using an enhanced Volume-of-Fluid (VOF) method. International Journal of Mechanical Sciences, 2022. 215.
24. Kraposhin, M., A. Bovtrikova, and S. Strijhak, Adaptation of Kurganov-Tadmor Numerical Scheme for Applying in Combination with the PISO Method in Numerical Simulation of Flows in a Wide Range of Mach Numbers. Procedia Computer Science, 2015. 66: p. 43–52.

 doi:10.20944/preprints202510.1743.v1

25. Gan, J., et al., Applicability research and experimental verification based on the coupling of turbulence model and mesh types to capture jet characteristics. Flow Measurement and Instrumentation, 2024. 98.
26. Fu, G., J. Jiang, and L. Ni, Research-scale three-phase jet foam generator design and foaming condition optimization based on Box–Behnken design. Process Safety and Environmental Protection, 2020. 134: p. 217–225.
27. Zou, Y., et al., Optimization of water spray parameters for an infrared suppression (IRS) device based on regression orthogonal design and AHP-entropy method. International Communications in Heat and Mass Transfer, 2025. 167.
28. Dong, Z., et al., Parameter identification and real-time motion prediction for a water-jet unmanned surface vehicle based on online sparse least squares support vector machine algorithm. Control Engineering Practice, 2025. 164.
29. Ramesh, M., et al., Evaluation and study of PBI reinforced with HDPE on abrasive wear using ANOVA and CODAS approach for protective shell applications. Journal of Pipeline Science and Engineering, 2025.
30. Carvalho, H.D.P.d., J.F.L.d. Oliveira, and R.A.d.A. Fagundes, Dynamic selection of ensemble-based regression models: Systematic literature review. Expert Systems with Applications, 2025. 290.
31. Sutowski, P., B. Zieliński, and K. Nadolny, Advanced regression model fitting to experimental results in case of the effect of grinding conditions on a cutting force with the planer technical knives. Measurement, 2025. 241.
32. Li, B., et al., Fluid-Structure interaction analysis of a 1000 MW supercritical Coal-Fired boiler Water-Cooled wall based on Multi-parameter simulation. Applied Thermal Engineering, 2025. 274.